# PHANGS–JWST First Results: The Influence of Stellar Clusters on Polycyclic Aromatic Hydrocarbons in Nearby Galaxies

Daniel A. Dale[1] , Médéric Boquien[2] , Ashley T. Barnes[3] , Francesco Belfiore[4] , Frank Bigiel[3] , Yixian Cao[5] ,
Rupali Chandar[6] , Jérémy Chastenet[7] , Mélanie Chevance[8] , Sinan Deger[9] , Oleg V. Egorov[10] , Kathryn Grasha[11,12] ,
Brent Groves[13] , Hamid Hassani[14] , Kiana F. Henny[1] , Ralf S. Klessen[8,15] , Kathryn Kreckel[10] ,
J. M. Diederik Kruijssen[16] , Kirsten L. Larson[17] , Janice C. Lee[18] , Adam K. Leroy[19] , Daizhong Liu[5] , Eric J. Murphy[20] ,
Erik Rosolowsky[14] , Karin Sandstrom[21] , Eva Schinnerer[22] , Jessica Sutter[21] , David A. Thilker[23] ,
Elizabeth J. Watkins[10] , Bradley C. Whitmore[24] , and Thomas G. Williams[22,25]

[1] Department of Physics and Astronomy, University of Wyoming, Laramie, WY 82071, USA; ddale@uwyo.edu
[2] Centro de Astronomía (CITEVA), Universidad de Antofagasta, Avenida Angamos 601, Antofagasta, Chile
[3] Argelander-Institut für Astronomie, Universität Bonn, Auf dem Hügel 71, D-53121, Bonn, Germany
[4] INAF—Arcetri Astrophysical Observatory, Largo E. Fermi 5, I-50125 Florence, Italy
[5] Max-Planck-Institut für Extraterrestrische Physik (MPE), Giessenbachstr. 1, D-85748 Garching, Germany
[6] Ritter Astrophysical Research Center, University of Toledo, Toledo, OH 43606, USA
[7] Sterrenkundig Observatorium, Universiteit Gent, Krijgslaan 281 S9, B-9000 Gent, Belgium
[8] Institut für Theoretische Astrophysik, Zentrum für die Astronomie der Universität Heidelberg, Albert-Ueberle-Strasse 2, D-69120 Heidelberg, Germany
[9] TAPIR, California Institute of Technology, Pasadena, CA 91125 USA
[10] Astronomisches Rechen-Institut, Zentrum für Astronomie der Universität Heidelberg, Mönchhofstr. 12-14, D-69120 Heidelberg, Germany
[11] Research School of Astronomy and Astrophysics, Australian National University, Canberra, ACT 2611, Australia
[12] ARC Centre of Excellence for All Sky Astrophysics in 3 Dimensions (ASTRO 3D), Australia
[13] International Centre for Radio Astronomy Research, University of Western Australia, 35 Stirling Highway, Crawley, WA 6009, Australia
[14] Department of Physics, University of Alberta, Edmonton, AB T6G 2E1, Canada
[15] Universität Heidelberg, Interdisziplinäres Zentrum für Wissenschaftliches Rechnen, Im Neuenheimer Feld 205, D-69120 Heidelberg, Germany
[16] Cosmic Origins Of Life (COOL) Research DAO, coolresearch.io.
[17] AURA for the European Space Agency (ESA), Space Telescope Science Institute, 3700 San Martin Drive, Baltimore, MD 21218, USA
[18] Gemini Observatory/NSF NOIRLab, 950 N. Cherry Avenue, Tucson, AZ 85719, USA
[19] Department of Astronomy, The Ohio State University, 140 West 18th Avenue, Columbus, OH 43210, USA
[20] National Radio Astronomy Observatory, 520 Edgemont Road, Charlottesville, VA 22903, USA
[21] Center for Astrophysics & Space Sciences, Department of Physics, University of California San Diego, 9500 Gilman Drive, La Jolla, CA 92093, USA
[22] Max Planck Institut für Astronomie, Königstuhl 17, D-69117 Heidelberg, Germany
[23] Department of Physics and Astronomy, The Johns Hopkins University, Baltimore, MD 21218 USA
[24] Space Telescope Science Institute, 3700 San Martin Drive, Baltimore, MD 21218, USA
[25] Sub-department of Astrophysics, Department of Physics, University of Oxford, Keble Road, Oxford OX1 3RH, UK

## Abstract

We present a comparison of theoretical predictions of dust continuum and polycyclic aromatic hydrocarbon (PAH) emission with new JWST observations in three nearby galaxies: NGC 628, NGC 1365, and NGC 7496. Our analysis focuses on a total of 1063 compact stellar clusters and 2654 stellar associations previously characterized by the Hubble Space Telescope in the three galaxies. We find that the distributions and trends in the observed PAH-focused infrared colors generally agree with theoretical expectations, and that the bulk of the observations is more aligned with models of larger, ionized PAHs. These JWST data usher in a new era of probing interstellar dust and studying how the intense radiation fields near stellar clusters and associations play a role in shaping the physical properties of PAHs.

*Unified Astronomy Thesaurus concepts:* Star clusters (1567); Polycyclic aromatic hydrocarbons (1280); Spiral galaxies (1560)

## 1. Introduction

Polycyclic aromatic hydrocarbon (PAHs) contribute as much as 20% of a star-forming galaxy's total infrared emission (Smith et al. 2007) and produce bright emission features in the mid-infrared (e.g., Tielens 2008) that have been used as star formation tracers across cosmic time (e.g., Riechers et al. 2014). However, PAH emission exhibits large variability within and between galaxies, and it is important to determine the factors that drive PAH properties and strength. Previous studies of PAH emission features in galaxies have shown that the strength of PAH emission is sensitive to the metal abundance of the interstellar medium (ISM), the molecular gas surface density, the hardness and strength of the interstellar radiation field (or related metrics such as the star formation rate, dust temperature, active galactic nucleus X-ray luminosity, etc.), or some combination thereof (e.g., Engelbracht et al. 2005; Madden et al. 2006; Wu et al. 2006; Draine et al. 2007; Engelbracht et al. 2008; Dale et al. 2009; Sandstrom et al. 2010; Wu et al. 2010; Rémy-Ruyer et al. 2015; Jensen et al. 2017; Chastenet et al. 2019; Aniano et al. 2020; Galliano et al. 2021; Wolfire et al. 2022). These studies that were completed using previous generations of space-based infrared facilities targeted bright peaks of infrared emission or averaged over
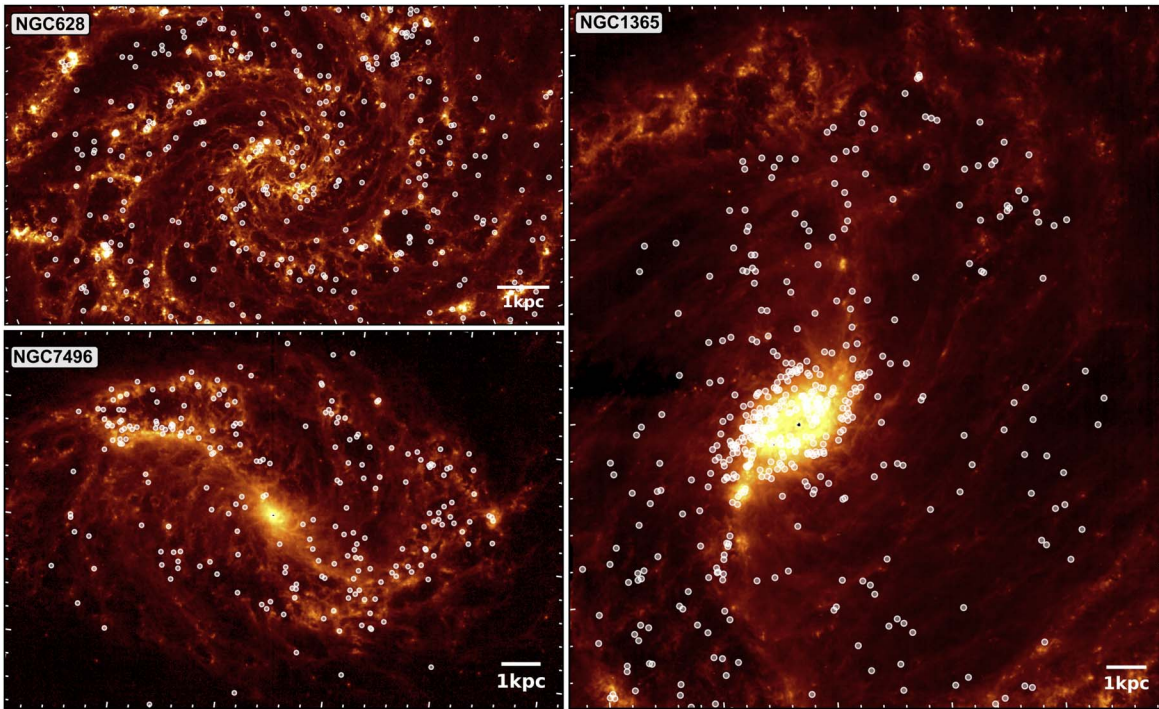
**Figure 1.** F770W imaging along with the locations of the stellar clusters. A 1 kpc scale bar is included within each panel.

large swaths of lower surface brightness regions. The advent of the more sensitive instruments on board JWST enable characterization of the PAH emission at high angular resolution across entire galaxy disks, including the 3.3 $\mu$m PAH feature that is essential to constraining the PAH size distribution but heretofore rarely observed for statistically significant samples (Lai et al. 2020, and references therein). Similarly, the relative strengths of PAH emission features, including those at 3.3, 7.7, and 11.2 $\mu$m, have long been thought to be critically dependent on the levels of PAH ionization (e.g., DeFrees & Miller 1989; Allamandola et al. 1999).

With JWST and the Hubble Space Telescope (HST) we present a novel study of the relationship between the strength of three key PAH mid-infrared features on the physical scales of star clusters and associations, and investigate trends with the ages of those stellar populations. Intense ultraviolet radiation from star clusters dominated by young OB stars will, for example, ionize or even destroy PAHs, which in turn will impact the local reddening curve, the efficiency of the heating of the neutral ISM, chemical reaction rates, etc. (Hollenbach & Tielens 1997; Draine et al. 2007; Tielens 2008; Wolfire et al. 2022). We compare the theoretical predictions for PAH emission features with photometric observations from JWST for the Physics at High Angular resolution in Nearby Galaxies (PHANGS) program on nearby galaxies (Leroy et al. 2021; Lee et al. 2022, 2023; Emsellem et al. 2022), using three filters with bandpasses that capture PAH emission features centered at 3.3, 7.7, and 11.2 $\mu$m. We specifically compare our observations with the predictions laid out in Draine et al. (2021; see also Rigopoulou et al. 2021) for a range of PAH ionization levels and size distributions in addition to a variety of interstellar radiation field intensities and ages of the stellar populations that drive the dust heating.

## 2. Sample and Data

The galaxies and observations analyzed here are drawn from the PHANGS project. The first wave of PHANGS–JWST data included a suite of NIRCam (Rieke et al. 2005) and MIRI (Rieke et al. 2015) imaging for three star-forming galaxies. NGC 628 is a grand-design spiral galaxy at 9.84 Mpc, and both NGC 1365 (19.57 Mpc) and NGC 7496 (18.72 Mpc) are barred spirals with Seyfert nuclei (distances are from Kourkchi & Tully 2017; Shaya et al. 2017; Anand et al. 2021a, 2021b). The NIRCam mosaics use the F200M, F300M, F335M, and F360M filters and the MIRI mosaics use the F770W, F1000W, F1130W, and F2100W filters. The technical description and postprocessing of the NIRCam and MIRI imaging for the PHANGS–JWST program is described in Lee et al. (2023).

The catalog of stellar clusters utilized here is from the PHANGS–HST program (Turner et al. 2021; Lee et al. 2022; Thilker et al. 2022); we restrict our analysis to the Class 1 and 2 clusters (Whitmore et al. 2021; Deger et al. 2022), which are either compact and centrally concentrated (Class 1) or compact and slightly asymmetric (Class 2). In lieu of using the catalog of asymmetric and multipeaked Class 3 stellar associations, which is comparatively incomplete since the PHANGS–HST pipeline was optimized for detecting single-peaked compact clusters, we utilize the PHANGS–HST catalog of stellar associations. These stellar associations, which are less likely to be gravitationally bound than Class 1 and 2 compact clusters (Whitmore et al. 2021), are derived from a watershed analysis that is based on $V$-band point-source detections and a 32 pc FWHM Gaussian smoothing, as presented in Lee et al. (2023) and Larson et al. (2022). The stellar masses and ages for the clusters and associations are based on spectral energy distribution fits to the five-band ultraviolet/optical PHANGS–HST data sets and span ~$10^{2.8-6.0} M_\odot$ and 1 Myr to 13 Gyr (see also Turner et al. 2021).

There are a total of $330 + 501 + 232 = 1063$ compact clusters and $1539 + 689 + 426 = 2654$ stellar associations in the publicly available catalogs that overlap with the PHANGS–JWST footprints for NGC 628, NGC 1365, and NGC 7496, respectively. As can be seen in Figure 1, these three galaxies are rich with mid-infrared emission throughout their disks; 95% of the compact clusters and 93% of the stellar associations show mid-infrared emission coincident with their locations in at least one of the three bandpasses.

We remove clusters and associations for which their mid-infrared photometry is potentially impacted by the saturation effects associated with the active galactic nuclei for NGC 1365 and NGC 7496. Following Hassani et al. (2023), we reject sources that overlap with regions where the amplitude of the modeled point-spread functions (PSFs), centered on the locations of the active galactic nuclei (AGNs), are $>0.1\%$ of the PSF maxima. These masked central regions span $0.32 \, \mathrm{kpc}^2$ and $0.33 \, \mathrm{kpc}^2$, respectively, for NGC 1365 and NGC 7496. This step removes 6 clusters and 21 associations for NGC 1365 near the AGN, and 12 clusters and 33 associations for NGC 7496. If we further require a stellar mass of $\log(M_*/M_\odot) > 3.3$ to align with our targeted median cluster mass sensitivity for JWST observations (Lee et al. 2022; Larson et al. 2022), then the cluster sample size drops another 5% and the association sample drops another 17%.

## 3. Analysis

Since our analysis relies on a combination of the F300M, 179 F335M, F360M, F770W, and F1130W images, all of the images were convolved with smoothing kernels following Aniano et al. (2011) to achieve the effective 0″37 angular resolution of the F1130W data. Continuum-subtracted 3.3 μm PAH maps (F335M$_{\mathrm{PAH}}$) are constructed using the method outlined in Sandstrom et al. (2023) that leverages the F300M and F360M imaging to infer the underlying continua. No continuum subtraction is carried out for the F770W or F1130W imaging since the stellar contributions at these wavelengths are minor and the dust emission appearing in these two bands is dominated by PAH features (Smith et al. 2007; Egorov et al. 2023; Hassani et al. 2023). Future work will explore the impact of using, for example, the F1000W imaging as a proxy for the wavelength-adjacent continuum for the F770W and F1130W bands.

Aperture photometry is carried out for each compact stellar cluster using an aperture radius of 0″3. The general trends discussed in Section 4 are unaffected by modifications to our choice for aperture radius. The photometry for each stellar association is a simple sum of the fluxes for each pixel within the association's defined polygon, the edges for which are based on the surface "brightness" of the smoothed tracer star maps (see Larson et al. 2022, for details). The choice of the 32 pc scale stellar association watershed maps matches well with the apertures utilized for the compact stellar clusters—for our galaxy sample's distances, 0″3 radii correspond to 14–28 pc. No local "background" subtraction is applied to the cluster or association photometry.

Draine et al. (2021) present various PAH band ratio diagrams for comparison with observations (e.g., see their Figure 16–21). Since the models of Draine et al. (2021) do not include contributions from stars, nebular lines, or other sources such as AGNs, in their analysis they employ a "clipping"
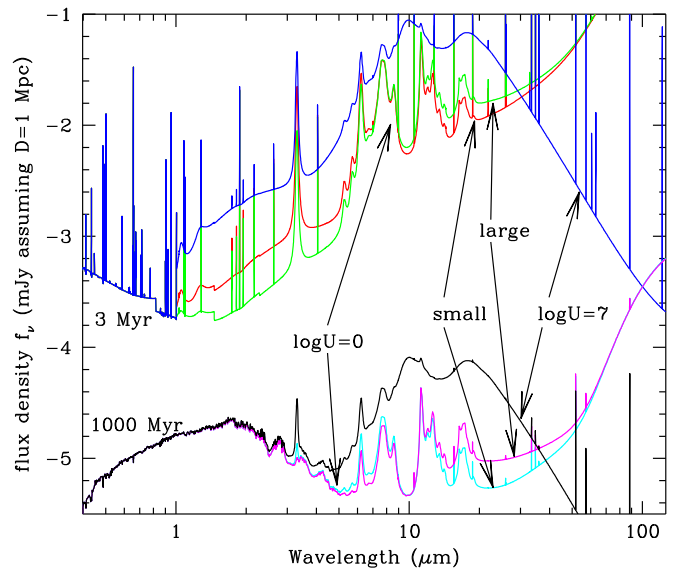


**Figure 2.** Example synthetic spectra drawn from the dust models of Draine et al. (2021) and generated using the CIGALE software (see Section 3 for details). The spectra are shown for maximum differences in the chosen grid for stellar age, PAH size, and interstellar radiation field intensity. The changes in the spectra as a function of PAH ionization are less pronounced and are thus not displayed. The six different colors represent the six different example spectra, with their physical properties indicated by arrows and their descriptors.

method to focus solely on the PAH emission features. Because our observed photometry in the JWST bandpasses inevitably include contributions from such other non-PAH sources of emission, we make direct comparisons with the models by extracting synthetic fluxes for each bandpass using the CIGALE software (Boquien et al. 2019) and the Draine et al. (2021) models as the input simulated spectra. To simulate a variety of conditions we construct a suite of simulated spectra that span a range of PAH ionizations (ion = 0, 1, 2; see Draine et al. 2021, Figure 9(b)), PAH size distributions (size = 0, 1, 2 corresponding to $a_{01} = 3, 4, 5$ Å; see Draine et al. 2021, Figure 9(a)), interstellar radiation field intensities $U$ (logU = 0–7), and age of the stellar population (age = 3, 10, 100, 1000 Myr). We assume solar metallicity (Bruzual & Charlot 2003) stellar populations with a standard Chabrier (2003) initial mass function. Six of these synthetic spectra, chosen to demonstrate the dynamic range available in the models, are shown in Figure 2. The other parameters in CIGALE are fixed since varying them does not significantly change our results or interpretation, e.g., opting for solar metallicity, a Lyman continuum photon escape fraction of 0, etc. Finally, we have applied to our synthetic data the prescription outlined in Sandstrom et al. (2023) for removing the underlying continuum to the 3.3 μm PAH feature emission, to be consistent with our treatment of the observations.

## 4. Results and Discussion

Figure 3 provides the F335M$_{\mathrm{PAH}}$/F1130W and F335M$_{\mathrm{PAH}}$/F770W band ratios for the three galaxies, where we use the shorthand notation "F335M$_{\mathrm{PAH}}$" to represent $\nu f_\nu$(F335M) for the PAH feature flux extracted for the F335M filter, etc. The data are color-coded according to stellar age. The two observed ratios each span about 1.4 dex, and they scale approximately linearly with each other; the numerators in the ratios are the same, and the denominators are comparable—thus the
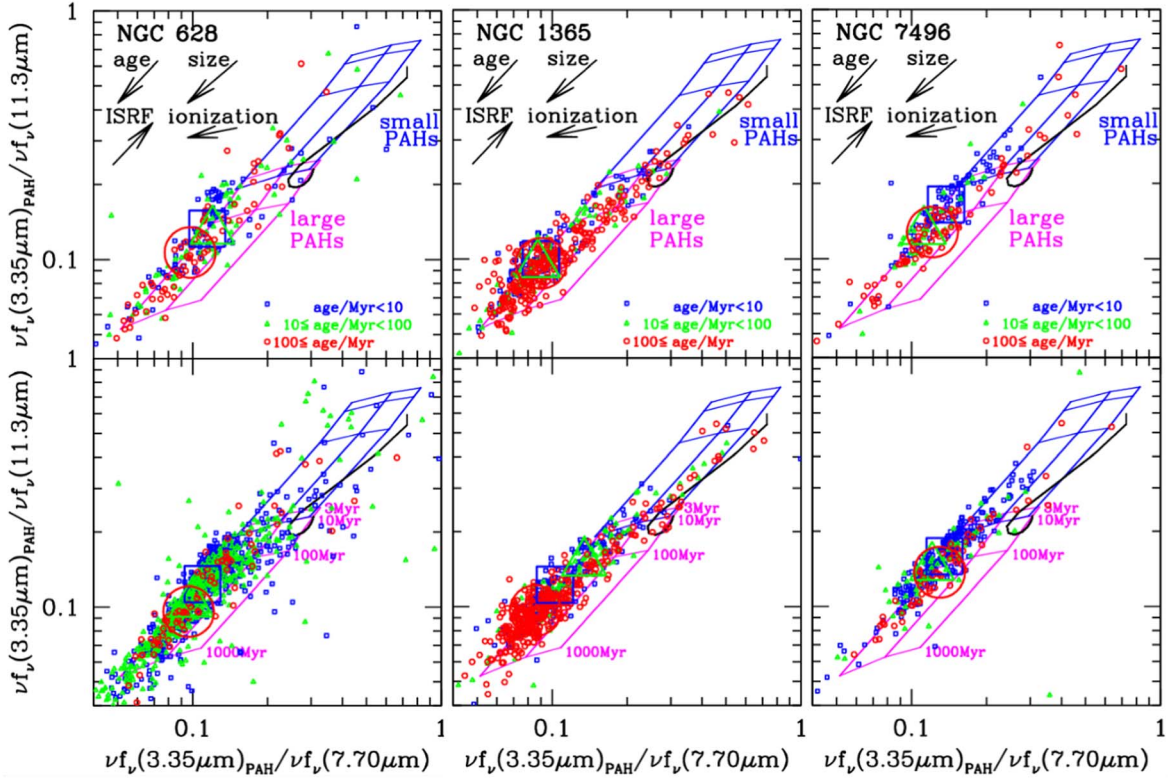
**Figure 3.** PAH bandpass flux ratios for the compact clusters (top) and stellar associations (bottom). The open blue squares, green triangles, and red circles are for compact stellar clusters, colored according to their ages: 0–10 Myr, 10–100 Myr, and >100 Myr, respectively. Large symbols indicate medians. Overlaid tracks are presented for select subsets of the simulated ratios, and the general trends for these tracks are indicated with the inset arrows/descriptions (see the text for details). The magenta and blue tracks are for small ($a_{01} = 3$ Å) and large ($a_{01} = 5$ Å) modeled PAH distributions, respectively, with both assuming `logU` $= 0$, `ion`$=0$, 1.2, and `age` $= 10$ Myr. The black hook-shaped track spans log $U = 0$, 7 and fixes `ion` $= 0$, `size` $= 2$, and `age` $= 10$ Myr.

**Table 1**
Statistics for Figure 3

| Galaxy | Population | Age/Myr < 10 | 10 ⩽ Age/Myr < 100 | 100 ⩽ Age/Myr | Probability |
|---|---|---|---|---|---|
| | | [a] $\mathrm{med}_x$,$\mathrm{med}_y$ $\mathrm{SIQR}_x$,$\mathrm{SIQR}_y$ | $\mathrm{med}_x$,$\mathrm{med}_y$ $\mathrm{SIQR}_x$,$\mathrm{SIQR}_y$ | $\mathrm{med}_x$,$\mathrm{med}_y$ $\mathrm{SIQR}_x$,$\mathrm{SIQR}_y$ | Kolm-Smir |
| NGC0628 | clusters | −0.94, −0.88 0.08,0.13 | −0.92, −0.88 0.12,0.15 | −1.01, −0.97 0.15,0.17 | $7 \cdot 10^{-3}$ |
| NGC0628 | associations | −0.96, −0.91 0.09,0.12 | −1.00, −0.99 0.13,0.15 | −1.02, −1.02 0.14,0.16 | $2 \cdot 10^{-4}$ |
| NGC1365 | clusters | −1.05, −1.00 0.08,0.08 | −1.06, −1.02 0.12,0.14 | −1.04, −1.02 0.11,0.10 | $1 \cdot 10^{-3}$ |
| NGC1365 | associations | −0.99, −0.91 0.11,0.12 | −0.87, −0.82 0.14,0.13 | −1.07, −1.02 0.09,0.07 | $6 \cdot 10^{-8}$ |
| NGC7496 | clusters | −0.86, −0.78 0.09,0.10 | −0.95, −0.89 0.09,0.09 | −0.92, −0.89 0.15,0.14 | $6 \cdot 10^{-4}$ |
| NGC7496 | associations | −0.87, −0.80 0.08,0.09 | −0.92, −0.84 0.12,0.09 | −0.89, −0.86 0.10,0.12 | $6 \cdot 10^{-3}$ |
| | | [b] $\mathrm{mean}_x$,$\mathrm{mean}_y$ $\sigma_x$,$\sigma_y$ | $\mathrm{mean}_x$,$\mathrm{mean}_y$ $\sigma_x$,$\sigma_y$ | $\mathrm{mean}_x$,$\mathrm{mean}_y$ $\sigma_x$,$\sigma_y$ | $t$-test |
| NGC0628 | clusters | −0.94, −0.89 0.22,0.24 | −0.88, −0.86 0.35,0.27 | −1.01, −0.97 0.36,0.37 | 0.16,0.10 |
| NGC0628 | associations | −0.96, −0.94 0.26,0.27 | −1.00, −1.00 0.29,0.30 | −1.03, −1.02 0.44,0.45 | 0.07,0.04 |
| NGC1365 | clusters | −1.02, −0.98 0.20,0.20 | −1.02, −1.00 0.27,0.28 | −0.99, −1.00 0.26,0.24 | 0.11,0.70 |
| NGC1365 | associations | −0.94, −0.90 0.22,0.22 | −0.87, −0.85 0.27,0.25 | −1.02, −1.00 0.26,0.26 | 0.03,0.0009 |
| NGC7496 | clusters | −0.89, −0.81 0.20,0.22 | −0.96, −0.91 0.18,0.20 | −0.85, −0.86 0.32,0.26 | 0.33,0.25 |
| NGC7496 | associations | −0.88, −0.81 0.17,0.18 | −0.89, −0.86 0.20,0.22 | −0.84, −0.82 0.23,0.23 | 0.26,0.63 |

**Notes.**
[a] $\mathrm{Med}_x$ and $\mathrm{med}_y$ refer to the medians of $\log_{10}(\mathrm{F335M_{PAH}/F770W})$ and $\log_{10}(\mathrm{F335M_{PAH}/F1130W})$, respectively. The semi-interquartile ranges are half the 25%–75% range found after sorting the flux ratios. The SIQRs provided here are in units of dex since they are computed using the (base 10) logarithms of the flux ratios. The Kolmogorov–Smirnov probabilities characterize how significantly the <10 Myr and >100 Myr two-dimensional distributions differ, with probabilities less than ∼0.05 indicating a significant difference (Press 1993).
[b] $\mathrm{Mean}_x$ and $\mathrm{mean}_y$ refer to the means of $\log_{10}(\mathrm{F335M_{PAH}/F770W})$ and $\log_{10}(\mathrm{F335M_{PAH}/F1130W})$, respectively; $\sigma$ indicates the standard deviation. $t$-test probabilities characterize how significantly the <10 Myr and >100 Myr (one-dimensional log$x$, log$y$) means differ, with probabilities less than ∼0.05 indicating significantly different values (Press 1993).

approximately one-to-one correlation seen in Figure 3. We provide in Table 1 the population medians and their semi-interquartile spreads in log base 10, along with the population means and their standard deviations. In addition, we provide the results of $t$-tests to quantify how significantly different are the population means. For the compact clusters in NGC 628 and NGC 7496 the medians and means for the F335M$_{PAH}$/F1130W and F335M$_{PAH}$/F770W ratios decrease with increasing stellar age as suggested by the synthetic model extractions described immediately below, particularly when comparing the <10 Myr and >100 Myr populations. For the stellar associations the overall distributions are consistent with what is observed for the compact clusters, and the older stellar populations show noticeably lower F335M$_{PAH}$/F1130W and F335M$_{PAH}$/F770W ratios in NGC 628 and NGC 1365. However, the $t$-test results imply that these differences are only statistically significant for the associations in NGC 628 and NGC 1365 and marginally significant for the clusters in NGC 628. Finally, we note that the scatter in the distributions increases with stellar age; the average semi-interquartile ranges for the young, intermediate, and old clusters and associations are 0.097, 0.122, and 0.124 dex, and the average standard deviations are 0.216, 0.256, and 0.307 dex, respectively, for the three age populations.

We also include in Figure 3 the grid of synthetic points from the models of Draine et al. (2021) described in Section 3. The magenta and blue grids in Figure 3 demonstrate how the synthetic points depend on stellar cluster age, PAH size distribution, and PAH ionization (after fixing $U = 1$). The black track portrays how the synthetic data vary with the intensity of the interstellar radiation field for $\log U = 0$–7 (after fixing ion $= 0$, size $= 2$, and age $= 10$ Myr). The large arrows and corresponding descriptors indicate how the synthetic tracks change with each modeled parameter; these synthetic trends are consistent with those portrayed in Figure 21(d) of Draine et al. (2021). The overall distributions of the observed ratios in Figure 3 track well with the displayed grid of synthetic models, and the majority of the observations are consistent with the PAHs having elevated ionization levels and large size distributions. In other words, the data are mostly populating the magenta grid for larger PAHs (and not the blue grid for smaller PAHs), between the magenta model tracks for 100 Myr and 1000 Myr, and the data are more closely aligned with the left-hand edge of the magenta grid that indicates more highly ionized PAHs. The implication is that the proximity of stellar clusters and associations has enhanced the photoejection of electrons from the PAHs.

Our evidence for higher levels of PAH ionization is conceptually consistent with the work of other PHANGS–JWST efforts appearing in this Issue. Egorov et al. (2023) analyze the F1130W/F770W parameter, widely considered to be a tracer of the ratio of neutral to ionized PAHs (Draine & Li 2001; Maragkoudakis et al. 2020), in H II regions in NGC 628, NGC 1365, NGC 7496, and IC 5332 and find lower values of F1130W/F770W in regions with higher [S III]/[S II] ratios, indicating harder radiation fields. Chastenet et al. (2023) probe PAH band ratios across the disks of the four galaxies and find evidence of hotter, highly ionized PAHs in the vicinity of H II regions that are defined by the radiation from young stars. Finally, Sandstrom et al. (2023) create maps of PAH band ratios in the same three galaxies considered in this work and find fairly flat F335M$_{PAH}$/F1130W radial profiles, with

amplitudes similar to what we find (0.07–0.24 in $\nu f_\nu$ units). A follow-up control study using a larger sample of PHANGS galaxies will compare the PAH ionization levels inferred in this work near stellar clusters and associations with those of PAHs that are spread throughout the diffuse ISM.

Close scrutiny of Figure 3 suggests subtle differences between galaxies, such as the sources in NGC 7496 being on average higher up in the magenta grid, which is consistent with more intense radiation fields (and/or young stellar ages). It is unlikely that the AGN in NGC 7496 is responsible for this difference, as we have removed the central clusters and associations from our analysis (see Section 2) and our stellar sources in NGC 7496 are dispersed throughout its disk and spiral arms (Figure 1). In addition, NGC 628 shows larger scatter in the data than for NGC 1365 and NGC 7496, with standard deviations in the abscissa and ordinate values larger by factors of 1.23, 1.30, and 1.56 for the <10 Myr, 10–100 Myr, and >100 Myr populations, respectively. The factor of 2 larger distances for NGC 1365 and NGC 7496 compared to the distance for NGC 628 result in more spatial averaging over the 0″.6 diameter aperture and thus the smaller scatter in the data.

## 5. Conclusions

We have leveraged new JWST near- and mid-infrared imaging of NGC 628, NGC 1365, and NGC 7496 to study their PAH emission. With the combined data from the three galaxies we are able to analyze the PAH emission over localized (<32 pc scale) regions centered on 1063 compact stellar clusters and 2654 stellar associations previously analyzed with HST ultraviolet/optical imaging. This study represents the first look at matched PAH band ratios, at high angular resolution, for large statistical samples of stellar ionizing sources isolated from more diffuse ISM conditions, enabling us to directly link ionizing sources to their impact on PAH properties across representative disk environments.

To enable a comparison with theoretical expectations, we extracted synthetic infrared colors based on models of stellar, PAH, and dust continuum emission. A full grid of synthetic values is created by modifying four key parameters: stellar age, PAH ionization fraction, PAH size distribution, and interstellar radiation field intensity. Our results are generally consistent with the predictions from the dust models outlined in Draine et al. (2021), though the PAH band ratios we measure for the youngest stellar clusters and associations (<10 Myr) appear between theoretical grid values (assuming large PAH size distributions) for stellar ages between 100 and 1000 Myr. In addition, we find statistical evidence for the stellar associations in NGC 628 and NGC 1365 having decreasing values of F335M$_{PAH}$/F1130W and F335M$_{PAH}$/F770W with increasing stellar age, consistent with the expectations based on the synthetic extractions. The slope and the overall distribution for the ensemble of synthetic PAH band ratios is consistent with that for the observed distributions in the three galaxies, and the models with higher levels of PAH ionization and larger size distributions are generally more aligned with the observations. A higher level of ionization could indicate enhanced processing of PAHs from the radiation fields produced by the stellar clusters. Finally, there is an age-dependent trend in the scatter, with older stellar populations exhibiting larger dispersions in the PAH band ratios.

Dale et al.

Further additional analysis with the full PHANGS–JWST sample is needed to more firmly test theoretical dust models. The larger PHANGS sample will enable us to explore PAH band ratios as a function of local metallicity and radiation hardness indicators, and thus bring additional insight into the dearth of PAHs for environments of depressed metal abundance and/or elevated radiation hardness. Furthermore, an analysis that leverages the larger PHANGS–JWST sample will provide a more robust sample for measuring PAH band ratios in diffuse regions as a control against which we will compare our measurements near stellar clusters and associations.

## ORCID iDs

Daniel A. Dale ⓘ https://orcid.org/0000-0002-5782-9093
Médéric Boquien ⓘ https://orcid.org/0000-0003-0946-6176
Ashley T. Barnes ⓘ https://orcid.org/0000-0003-0410-4504
Francesco Belfiore ⓘ https://orcid.org/0000-0002-2545-5752
Frank Bigiel ⓘ https://orcid.org/0000-0003-0166-9745
Yixian Cao ⓘ https://orcid.org/0000-0001-5301-1326
Rupali Chandar ⓘ https://orcid.org/0000-0003-0085-4623
Jérémy Chastenet ⓘ https://orcid.org/0000-0002-5235-5589
Mélanie Chevance ⓘ https://orcid.org/0000-0002-5635-5180
Sinan Deger ⓘ https://orcid.org/0000-0003-1943-723X
Oleg V. Egorov ⓘ https://orcid.org/0000-0002-4755-118X
Kathryn Grasha ⓘ https://orcid.org/0000-0002-3247-5321
Brent Groves ⓘ https://orcid.org/0000-0002-9768-0246
Hamid Hassani ⓘ https://orcid.org/0000-0002-8806-6308
Kiana F. Henny ⓘ https://orcid.org/0000-0001-7448-1749
Ralf S. Klessen ⓘ https://orcid.org/0000-0002-0560-3172
Kathryn Kreckel ⓘ https://orcid.org/0000-0001-6551-3091
J. M. Diederik Kruijssen ⓘ https://orcid.org/0000-0002-8804-0212
Kirsten L. Larson ⓘ https://orcid.org/0000-0003-3917-6460
Janice C. Lee ⓘ https://orcid.org/0000-0002-2278-9407
Adam K. Leroy ⓘ https://orcid.org/0000-0002-2545-1700
Daizhong Liu ⓘ https://orcid.org/0000-0001-9773-7479
Eric J. Murphy ⓘ https://orcid.org/0000-0001-7089-7325
Erik Rosolowsky ⓘ https://orcid.org/0000-0002-5204-2259
Karin Sandstrom ⓘ https://orcid.org/0000-0002-4378-8534
Eva Schinnerer ⓘ https://orcid.org/0000-0002-3933-7677
Jessica Sutter ⓘ https://orcid.org/0000-0002-9183-8102
David A. Thilker ⓘ https://orcid.org/0000-0002-8528-7340
Elizabeth J. Watkins ⓘ https://orcid.org/0000-0002-7365-5791
Bradley C. Whitmore ⓘ https://orcid.org/0000-0002-3784-7032
Thomas G. Williams ⓘ https://orcid.org/0000-0002-0012-2142

## References

Allamandola, L. J., Hudgins, D. M., & Sandford, S. A. 1999, ApJL, 511, L115
Anand, G. S., Lee, J. C., Van Dyk, S. D., et al. 2021a, MNRAS, 501, 3621
Anand, G. S., Rizzi, L., Tully, R. B., et al. 2021b, AJ, 162, 80
Aniano, G., Draine, B. T., Gordon, K. D., & Sandstrom, K. 2011, PASP, 123, 1218
Aniano, G., Draine, B. T., Hunt, L. K., et al. 2020, ApJ, 889, 150
Boquien, M., Burgarella, D., Roehlly, Y., et al. 2019, A&A, 622, A103
Bruzual, G., & Charlot, S. 2003, MNRAS, 344, 1000
Chabrier, G. 2003, PASP, 115, 763
Chastenet, J., Leroy, A., Schinnerer, E., et al. 2023, ApJL, 944, L12
Chastenet, J., Sandstrom, K., Chiang, I.-D., et al. 2019, ApJ, 876, 62
Dale, D. A., Cohen, S. A., Johnson, L. C., et al. 2009, ApJ, 703, 517

DeFrees, D. J., & Miller, M. D. 1989, in IAU Symp. 135, Interstellar Dust, ed. L. J. Allamandola & A. G. G. M. Tielens (Cambridge: Cambridge Univ. Press), 173

Deger, S., Lee, J. C., Whitmore, B. C., et al. 2022, MNRAS, 510, 32

Draine, B. T., Dale, D. A., Bendo, G., et al. 2007, ApJ, 663, 866

Draine, B. T., & Li, A. 2001, ApJ, 551, 807

Draine, B. T., Li, A., Hensley, B. S., et al. 2021, ApJ, 917, 3

Egorov, D., Leroy, A., Schinnerer, E., et al. 2023, ApJL, 944, L16

Emsellem, E., Schinnerer, E., Santoro, F., et al. 2022, A&A, 659, A191

Engelbracht, C. W., Gordon, K. D., Rieke, G. H., et al. 2005, ApJL, 628, L29

Engelbracht, C. W., Rieke, G. H., Gordon, K. D., et al. 2008, ApJ, 678, 804

Galliano, F., Nersesian, A., Bianchi, S., et al. 2021, A&A, 649, A18

Hassani, H., Rosolowsky, E. W., Leroy, A. K., et al. 2023, ApJL, 944, L21

Hollenbach, D. J., & Tielens, A. G. G. M. 1997, ARA&A, 35, 179

Jensen, J. J., Hönig, S. F., Rakshit, S., et al. 2017, MNRAS, 470, 3071

Kourkchi, E., & Tully, R. B. 2017, ApJ, 843, 16

Lai, T. S. Y., Smith, J. D. T., Baba, S., Spoon, H. W. W., & Imanishi, M. 2020, ApJ, 905, 55

Larson, K. L. 2022, MNRAS, submitted

Lee, J., Sandstrom, K. M., Leroy, A. K., et al. 2023, ApJL, 944, L17

Lee, J. C., Whitmore, B. C., Thilker, D. A., et al. 2022, ApJS, 258, 10

Leroy, A. K., Schinnerer, E., Hughes, A., et al. 2021, ApJS, 257, 43

Madden, S. C., Galliano, F., Jones, A. P., & Sauvage, M. 2006, A&A, 446, 877

Maragkoudakis, A., Peeters, E., & Ricca, A. 2020, MNRAS, 494, 642

Press, W. H. 1993, Sci, 259, 1931

Rémy-Ruyer, A., Madden, S. C., Galliano, F., et al. 2015, A&A, 582, A121

Riechers, D. A., Pope, A., Daddi, E., et al. 2014, ApJ, 786, 31

Rieke, G. H., Wright, G. S., Böker, T., et al. 2015, PASP, 127, 584

Rieke, M. J., Kelly, D., & Horner, S. 2005, Proc. SPIE, 5904, 1

Rigopoulou, D., Barale, M., Clary, D. C., et al. 2021, MNRAS, 504, 5287

Sandstrom, K., Koch, E. W., Leroy, A. K., et al. 2023, ApJL, 944, L8

Sandstrom, K. M., Bolatto, A. D., Draine, B. T., Bot, C., & Stanimirović, S. 2010, ApJ, 715, 701

Shaya, E. J., Tully, R. B., Hoffman, Y., & Pomarède, D. 2017, ApJ, 850, 207

Smith, J. D. T., Draine, B. T., Dale, D. A., et al. 2007, ApJ, 656, 770

Thilker, D. A., Whitmore, B. C., Lee, J. C., et al. 2022, MNRAS, 509, 4094

Tielens, A. G. G. M. 2008, ARA&A, 46, 289

Turner, J. A., Dale, D. A., Lee, J. C., et al. 2021, MNRAS, 502, 1366

Whitmore, B. C., Lee, J. C., Chandar, R., et al. 2021, MNRAS, 506, 5294

Wolfire, M. G., Vallini, L., & Chevance, M. 2022, ARA&A, 60, 247

Wu, Y., Charmandaris, V., Hao, L., et al. 2006, ApJ, 639, 157

Wu, Y., Helou, G., Armus, L., et al. 2010, ApJ, 723, 895